J. Fluid Mech. (1992), *vol.* 245, *pp.* 211–227

Dynamic permeability: reformulation of theory and new experimental and numerical data

By D. M. J. SMEULDERS, R. L. G. M. EGGELS AND M. E. H. VAN DONGEN

Eindhoven University of Technology, PO Box 513, 5600 MB Eindhoven, The Netherlands

(Received 24 September 1991 and in revised form 5 February 1992)

The dynamic interaction between a rigid porous structure (porosity ϕ) and its saturating fluid is studied. From the microscopic conservation laws and constitutive relations, macroscopic equations are derived. An averaging technique proposed and discussed by for example Lévy, Auriault and Burridge & Keller is used, from which we reformulate the theory by Johnson, Koplik & Dashen. The macroscopic equations then serve to describe the high-frequency behaviour of an oscillating fluid within a porous sample. This behaviour may be characterized by the length parameter Λ and by the tortuosity parameter α_∞. It is shown that Λ and α_∞, which describe an oscillatory flow behaviour, may be evaluated on the basis of steady potential flow theory. Numerical results are then presented for several pore geometries, and for these geometries, the steady-state permeability k_0 is computed numerically also. The parameter $8\alpha_\infty k_0/\phi\Lambda^2$, first introduced by Johnson *et al.*, is then evaluated and appears to be weakly dependent on pore geometry. This implies that for many porous media the dynamic interaction is described by an approximate scaling function. New experimental data, concerning oscillating flows through several porous media, are presented. Within limits of accuracy, these data are in agreement with the approximate scaling function.

1. Introduction

There are many technological areas for which it is interesting to know how fluid flows through porous media. The dynamic permeability $k(\omega)$ and the dynamic tortuosity $\alpha(\omega)$ are important properties to describe the macroscopic flow through porous media subjected to an oscillatory pressure gradient. Introducing an exp $(-\mathrm{i}\omega t)$ dependence for the fluid pressure p and the macroscopic fluid velocity v_0, $k(\omega)$ and $\alpha(\omega)$ are defined by

$$\frac{\eta\phi}{k(\omega)}\hat{v}_0 = -\nabla\hat{p}, \tag{1}$$

$$-\mathrm{i}\omega\rho_f\alpha(\omega)\hat{v}_0 = -\nabla\hat{p}. \tag{2}$$

In these two expressions, η is the fluid viscosity, ρ_f the fluid density and ϕ the porosity. In the past few years, many authors have attempted to express the macroscopic fluid behaviour in terms of averaged microscopic equations. Various authors have considered the steady-state permeability k_0 for stationary flow (Larson & Higdon 1989; Beasley & Torquato 1988; Rubinstein & Torquato 1989; Mei & Auriault 1991). The steady-state permeability is a real-valued quantity, defined by

$$\lim_{\omega\to 0} k(\omega) = k_0. \tag{3}$$

For the dynamic permeability $k(\omega)$, however, fewer results are available. Lévy (1979), Auriault (1980) and Burridge & Keller (1981) derived a two-scale homogenization formalism to describe the dynamical behaviour of a Newtonian fluid within a porous, elastic, medium. This dynamical behaviour is expressed in terms of averaged microscopic equations. Auriault, Borne & Chambon (1985) were the first to present both numerical and experimental data for a schematized, periodic, porous medium. They compared their results to an asymptotic, high-frequency, approximation. In 1987, Johnson, Koplik & Dashen described the dynamic permeability behaviour over the entire frequency range by a scaling function. They argue that the reduced dynamic permeability $k(\omega)/k_0$ must depend on a reduced frequency ω/ω_c, where ω_c is a rollover frequency from a viscosity-dominated regime to an inertia-dominated one:

$$\omega_c = \eta\phi/\rho_f k_0 \alpha_\infty, \tag{4}$$

where α_∞ is the tortuosity, defined by

$$\lim_{\omega\to\infty} \alpha(\omega) = \alpha_\infty. \tag{5}$$

By analysing the behaviour for high frequencies, Johnson *et al.* (1987) also found that $k(\omega)/k_0$ must be a function of yet another parameter

$$M = 8\alpha_\infty k_0/\phi\Lambda^2, \tag{6}$$

where Λ is an independently measurable property of a porous material with the dimension of length. In the same paper the parameter M is suggested to equal 1 for all porous media, at least approximately. So many porous media satisfy the simple approximate scaling law that $k(\omega)/k_0$ is a function of only one independent parameter ω/ω_c. All this was also briefly commented upon later (Johnson 1989). The assumption that there exists only one scaling function for all porous media was validated in later years, both numerically and experimentally. Numerical computations of the dynamic permeability for a variety of microstructures were presented by Sheng & Zhou (1988) and Yavari & Bedford (1990). Experimental data were obtained by Charlaix, Kushnick & Stokes (1988).

In this paper, three subjects will be treated. First, we will derive, from microstructure, the averaged dynamic permeability relations already presented by Lévy (1979), Auriault (1980) and Burridge & Keller (1981). Our relations are simplified somewhat because we have assumed the porous medium to be rigid. The unique macroscopic dynamic permeability $k(\omega)/k_0$, presented by Johnson *et al.* (1987), is then expressed in terms of averaged microscopic relations. High-frequency behaviour is studied.

Secondly, we will present a method for the numerical computation of the constituents of the parameter M given in (6). Two different axisymmetrical pore geometries will be considered, and values of M for different geometries will be given. Thirdly, we will present new experimental dynamic permeability data and compare these to the scaling function proposed by Johnson *et al.* (1987).

2. Microstructural approach

The microstructure of a random porous medium is generally characterized by a lengthscale a that is typical of the pore size. An extended statistical characterization in terms of various kinds of correlation functions has been considered by several authors (Rubinstein & Torquato 1989; Bear & Bachmat 1990). Another scale of

description is the macroscopic level, at which measurable continuous and differentiable quantities may be identified and boundary-value problems can be stated and solved. Its lengthscale is called L. We now define ϵ as a/L. Considering a rigid fluid-filled porous medium, we may write the linearized microscopic fluid equations:

$$\rho_f \frac{\partial \boldsymbol{u}}{\partial t} = -\nabla p + \eta \nabla^2 \boldsymbol{u} + (\eta + \eta')\,\nabla(\nabla \cdot \boldsymbol{u}), \tag{7}$$

$$\frac{1}{K_f}\frac{\partial p}{\partial t} = -\nabla \cdot \boldsymbol{u}, \tag{8}$$

where η' is the fluid dilatation viscosity and K_f is the fluid bulk modulus. Substitution of an $\exp(-i\omega t)$ dependence for the pressure p and fluid velocity $\boldsymbol{u}$ yields

$$-i\omega\rho_f \hat{\boldsymbol{u}} = -\nabla \hat{p} + \eta \nabla^2 \hat{\boldsymbol{u}} + (\eta + \eta')\,\nabla(\nabla \cdot \hat{\boldsymbol{u}}), \tag{9}$$

$$-i\omega \hat{p}/K_f = -\nabla \cdot \hat{\boldsymbol{u}}. \tag{10}$$

Equations (9) and (10) may be written in dimensionless form by introducing reference parameters $u_{\text{ref}} = \eta/\rho_f a$, $p_{\text{ref}} = L\eta^2/\rho_f a^3$, $\omega_{\text{ref}} = \eta/\rho_f a^2$ and $t_{\text{ref}} = 1/\omega_{\text{ref}}$:

$$-i\tilde{\omega}\tilde{\boldsymbol{u}} = -\frac{1}{\epsilon}\tilde{\nabla}\tilde{p} + \tilde{\nabla}^2\tilde{\boldsymbol{u}} + (1 + \eta'/\eta)\,\tilde{\nabla}(\tilde{\nabla} \cdot \tilde{\boldsymbol{u}}), \tag{11}$$

$$i\tilde{\omega}\tilde{p} = (1/\epsilon)\,\tilde{\nabla} \cdot \tilde{\boldsymbol{u}}, \tag{12}$$

where $\tilde{\nabla} = a\nabla$.

We may now apply the well-known technique of homogenization (Lévy 1979; Auriault 1980; Burridge & Keller 1981), involving the explicit recognition of two lengthscales in the problem by writing all quantities as a function of ϵ and the two spatial variables $\boldsymbol{x} = \boldsymbol{r}/L$ and $\boldsymbol{y} = \boldsymbol{r}/a$, and then expanding them as a perturbation series in ϵ. Furthermore, the gradient operator ∇ acts on both the x- and y-scales:

$$\tilde{\boldsymbol{u}} = \boldsymbol{u}_0(\boldsymbol{x}, \boldsymbol{y}) + \epsilon \boldsymbol{u}_1(\boldsymbol{x}, \boldsymbol{y}) + \ldots, \tag{13}$$

$$\tilde{p} = p_0(\boldsymbol{x}, \boldsymbol{y}) + \epsilon p_1(\boldsymbol{x}, \boldsymbol{y}) + \ldots, \tag{14}$$

$$\tilde{\nabla} = \epsilon \nabla_x + \nabla_y. \tag{15}$$

Note that for convenience the tilde has been omitted in the right-hand sides of the above equations. By now equating terms with equal powers of ϵ we obtain

$$-i\tilde{\omega}\boldsymbol{u}_0 = -\nabla_x p_0 - \nabla_y p_1 + \nabla_y^2 \boldsymbol{u}_0, \tag{16}$$

$$\nabla_y p_0 = 0, \tag{17}$$

$$i\tilde{\omega} p_0 = \nabla_x \cdot \boldsymbol{u}_0 + \nabla_y \cdot \boldsymbol{u}_1, \tag{18}$$

$$\nabla_y \cdot \boldsymbol{u}_0 = 0. \tag{19}$$

Similar equations were found by Lévy (1979) and Auriault (1980). Equation (17) indicates that the pressure p_0 is a function of the x spatial variable only and can therefore be identified as a measurable macroscopic quantity. Equation (19) indicates that the fluid may be regarded as incompressible on the microscopic level (y-scale). As pressure and velocity are complex-valued quantities, we may write from (16)

$$i\tilde{\omega}\boldsymbol{u}_0^* = -\nabla_x p_0^* - \nabla_y p_1^* + \nabla_y^2 \boldsymbol{u}_0^*. \tag{20}$$

The asterisk denotes complex-conjugated quantities. Multiplication of (16) and (20) by $\boldsymbol{u}_0^*$ and $\boldsymbol{u}_0$, respectively, and subsequent addition yields

$$-\nabla_y \cdot (p_1 \boldsymbol{u}_0^* + p_1^* \boldsymbol{u}_0) + \boldsymbol{u}_0^* \cdot \nabla_y^2 \boldsymbol{u}_0 + \boldsymbol{u}_0 \cdot \nabla_y^2 \boldsymbol{u}_0^* = \boldsymbol{u}_0^* \cdot \nabla_x p_0 + \boldsymbol{u}_0 \cdot \nabla_x p_0^*. \tag{21}$$

In order to link this microscopic equation to its macroscopic equivalent we shall average it over the y-variable. Aiming to define the average of any function g, defined for y in the fluid domain D_f, we will use the technique proposed by Burridge & Keller (1981). We consider a sphere $\mathscr{R}$ of radius R and integrate g with respect to y over that part of D_f which is contained in $\mathscr{R}$, and divide this integral by the volume of $\mathscr{R}$. Finally, taking the limit of this ratio as $R \to \infty$ we call this limit $\langle g(x) \rangle$. Applying this procedure to (21) we find

$$\langle \boldsymbol{u}_0^* \cdot \nabla_y^2 \boldsymbol{u}_0 + \boldsymbol{u}_0 \cdot \nabla_y^2 \boldsymbol{u}_0^* \rangle$$

$$= \langle \boldsymbol{u}_0^* \cdot \nabla_x p_0 + \boldsymbol{u}_0 \cdot \nabla_x p_0^* \rangle + \lim_{R \to \infty} \frac{1}{\frac{4}{3}\pi R^3} \int_{S_{fR}} (p_1 \boldsymbol{u}_0^* + p_1^* \boldsymbol{u}_0) \cdot \boldsymbol{n} \, \mathrm{d}y \, \mathrm{d}y. \quad (22)$$

The surface S_{fR} consists of two parts: the part of the pore surface within $\mathscr{R}$: $(S_f)_R$, and the part of the surface of the sphere $\mathscr{R}$ within D_f: $(S_R)_f$. Since the entire surface of the sphere is $4\pi R^2$, the integral over it is bounded by some constant times R^2. When divided by R^3 this integral is zero as $R \to \infty$. Therefore, the surface of integration in (22) may be replaced by $(S_f)_R$. Considering this surface, we find any fluid velocity perpendicular to the pore surface $(S_f)_R$ to be zero, and we are left with

$$\langle \boldsymbol{u}_0^* \cdot \nabla_y^2 \boldsymbol{u}_0 + \boldsymbol{u}_0 \cdot \nabla_y^2 \boldsymbol{u}_0^* \rangle = \langle \boldsymbol{u}_0^* \cdot \nabla_x p_0 + \boldsymbol{u}_0 \cdot \nabla_x p_0^* \rangle. \quad (23)$$

Defining the macroscopic fluid velocity $\tilde{\boldsymbol{v}}_0 = \langle \tilde{\boldsymbol{u}}_0 \rangle$, this equation may be rewritten:

$$\langle \tilde{\boldsymbol{u}}_0^* \cdot \tilde{\nabla}_y^2 \tilde{\boldsymbol{u}}_0 + \tilde{\boldsymbol{u}}_0 \cdot \tilde{\nabla}_y^2 \tilde{\boldsymbol{u}}_0^* \rangle = \tilde{\boldsymbol{v}}_0^* \cdot \tilde{\nabla}_x \tilde{p}_0 + \tilde{\boldsymbol{v}}_0 \cdot \tilde{\nabla}_x \tilde{p}_0^*. \quad (24)$$

We have reintroduced the tilde to focus attention on the dimensionless character of the quantities under consideration. The left-hand side of (24) is the averaged microscopic fluid response to the applied macroscopic pressure gradients on the right-hand side. However, this linear (i.e. small-amplitude) response of the pore fluid is usually described in terms of the macroscopic fluid velocity $\tilde{\boldsymbol{v}}_0 \mathrm{e}^{-\mathrm{i}\omega t}$ and the dynamic frequency-dependent tortuosity $\alpha(\omega)$. This relation was given by (2):

$$-\mathrm{i}\omega\alpha(\omega)\rho_f \hat{\boldsymbol{v}}_0 = -\nabla_x \hat{p}_0. \quad (25)$$

It is noted by comparing (1) and (2) that $\alpha(\omega)$ and $k(\omega)$ are not independent: $\alpha(\omega)/\alpha_\infty = \mathrm{i}k_0 \omega_c / \omega k(\omega)$. In dimensionless form (25) becomes

$$-\mathrm{i}\tilde{\omega}\alpha(\omega)\tilde{\boldsymbol{v}}_0 = -\tilde{\nabla}_x \tilde{p}_0. \quad (26)$$

As $\alpha(\omega)$ is a complex-valued quantity we may write from (26)

$$\mathrm{i}\tilde{\omega}\alpha^*(\omega)\tilde{\boldsymbol{v}}_0^* = -\tilde{\nabla}_x \tilde{p}_0^*. \quad (27)$$

Multiplication of (26) and (27) by $\tilde{\boldsymbol{v}}_0^*$ and $\tilde{\boldsymbol{v}}_0$, respectively, and subsequent addition yields an energy equation at the macroscopic level:

$$-2\,\mathrm{Im}\{\alpha(\omega)\}\tilde{\omega}|\tilde{\boldsymbol{v}}_0|^2 = \tilde{\boldsymbol{v}}_0^* \cdot \tilde{\nabla}_x \tilde{p}_0 + \tilde{\boldsymbol{v}}_0 \cdot \tilde{\nabla}_x \tilde{p}_0^*. \quad (28)$$

In (24), the fluid response to the applied pressure gradients is written in terms of averaged microscopic velocities. In (28), on the other hand, the fluid response to the applied macroscopic pressure gradients is written in terms of the macroscopic tortuosity $\alpha(\omega)$. We may now equate (24) and (28) to express $\alpha(\omega)$ in terms of ratios of averaged microscopic quantities:

$$\mathrm{Im}\{\alpha(\omega)\} = -\frac{\langle \tilde{\boldsymbol{u}}_0^* \cdot \tilde{\nabla}_y^2 \tilde{\boldsymbol{u}}_0 + \tilde{\boldsymbol{u}}_0 \cdot \tilde{\nabla}_y^2 \tilde{\boldsymbol{u}}_0^* \rangle}{2\tilde{\omega}|\tilde{\boldsymbol{v}}_0|^2}. \quad (29)$$

We note that the right-hand side of (29) is, in fact, only determined by the frequency and by the pore geometry because of the proportionality between all velocities involved. After some algebraic manipulations and reintroducing dimensions we may write

$$\mathrm{Im}\{\alpha(\omega)\} = -\frac{\eta}{2\omega\rho_f|\boldsymbol{v}_0|^2}\left\langle \frac{\partial}{\partial y_i}\left(u_{0j}^*\frac{\partial u_{0j}}{\partial y_i}+u_{0j}\frac{\partial u_{0j}^*}{\partial y_i}\right)-2\frac{\partial u_{0j}^*}{\partial y_i}\frac{\partial u_{0j}}{\partial y_i}\right\rangle, \tag{30}$$

where summation over repeated indices is assumed.

Replacing at the appropriate places in the previous derivation the addition by a subtraction, we may derive an expression for the real part of $\alpha(\omega)$ in a quite identical way:

$$\mathrm{Re}\{\alpha(\omega)\} = \frac{\langle|\tilde{\boldsymbol{u}}_0|^2\rangle}{|\tilde{\boldsymbol{v}}_0|^2}+\frac{\langle\tilde{\boldsymbol{u}}_0^*\cdot\tilde{\nabla}_y^2\tilde{\boldsymbol{u}}_0-\tilde{\boldsymbol{u}}_0\cdot\tilde{\nabla}_y^2\tilde{\boldsymbol{u}}_0^*\rangle}{2\mathrm{i}\tilde{\omega}|\tilde{\boldsymbol{v}}_0|^2}, \tag{31}$$

or alternatively

$$\mathrm{Re}\{\alpha(\omega)\} = \frac{\langle|\boldsymbol{u}_0|^2\rangle}{|\boldsymbol{v}_0|^2}+\frac{\eta}{2\mathrm{i}\omega\rho_f|\boldsymbol{v}_0|^2}\left\langle \frac{\partial}{\partial y_i}\left(u_{0j}^*\frac{\partial u_{0j}}{\partial y_i}-u_{0j}\frac{\partial u_{0j}^*}{\partial y_i}\right)\right\rangle. \tag{32}$$

3. High-frequency behaviour

Having written the imaginary and real parts of $\alpha(\omega)$ in this way ((30) and (32)), we may now investigate the high-frequency behaviour of $\alpha(\omega)$. In the limit of high frequencies, the viscous skin depth $\delta = (2\eta/\omega\rho_f)^{\frac{1}{2}}$ eventually becomes much smaller than any characteristic pore size. Any vorticity, $\nabla\times\boldsymbol{u}$, generated at the pore walls decays to zero as one moves away from the walls into the bulk of the pore. Therefore, except for a boundary layer of thickness δ, the fluid motion is given by potential flow, $\boldsymbol{u} = -\nabla_y\psi$, for some ψ. Below, we shall show that for an ideal fluid the quantity $\alpha(\omega)$ is a real-valued quantity α_∞, independent of fluid properties. Then we shall relate, exactly, the corrections to this extreme high-frequency limit α_∞ to the microscopic potential flow field for high frequencies. We note that since δ is arbitrarily small at high enough frequencies the walls of the pores appear to be flat in the boundary region. Therefore, introducing a boundary-layer velocity $\boldsymbol{u}_{0\delta}$ at a distance δ from the pore walls, the entire velocity field in the boundary layer is described by (Landau & Lifshitz 1959, p. 91)

$$\boldsymbol{u}_0 = \boldsymbol{u}_{0\delta}[1-\mathrm{e}^{\mathrm{i}k\beta}]. \tag{33}$$

In this equation, β is a local coordinate, measured from the pore wall into the bulk of the pore, and $k = (1+\mathrm{i})/\delta$ is the shear wavenumber at frequency ω. By substituting (33) into (32), the second term in the right-hand side of (32) vanishes and we readily arrive at ($\omega\to\infty$):

$$\mathrm{Re}\{\alpha(\omega)\} = \langle|\boldsymbol{u}_0|^2\rangle/|\boldsymbol{v}_0|^2. \tag{34}$$

Obviously, in the extreme high-frequency limit, the viscous skin depth δ tends to zero and we may write

$$\lim_{\omega\to\infty}\mathrm{Re}\{\alpha(\omega)\} = \alpha_\infty = \langle|\boldsymbol{u}_\mathrm{p}|^2\rangle/|\boldsymbol{v}_0|^2, \tag{35}$$

where $\boldsymbol{u}_\mathrm{p}$ is the potential flow solution. In Appendix A, we show that the high-frequency behaviour of $\mathrm{Re}\{\alpha(\omega)\}$, asymptotically approaching its extreme high-frequency limit α_∞, may be described by rewriting (34) in terms of this extreme high-frequency limit α_∞ and the viscous skin depth $\delta(\omega)$ ($\omega\to\infty$):

$$\mathrm{Re}\{\alpha(\omega)\} = \alpha_\infty[1+(1/\Lambda_1)\,\delta(\omega)]. \tag{36}$$

It is also shown in Appendix A that Λ_1 has the dimension of length, and can be evaluated on the basis of steady potential flow theory:

$$\frac{2}{\Lambda_1} = \frac{\left[(\partial/\partial r)\int |\boldsymbol{u}_\mathrm{p}|^2 \,\mathrm{d}V\right]_{\Delta\psi}}{\int |\boldsymbol{u}_\mathrm{p}|^2 \,\mathrm{d}V}. \tag{37}$$

In this equation, we have defined a flow potential difference $\Delta\psi$ between two arbitrary equipotential surfaces. Furthermore, $[(\partial/\partial r)\,G]_{\Delta\psi}$ denotes the derivative of some quantity G with respect to some outward virtual displacement r of the pore walls at constant $\Delta\psi$.

Next, we shall evaluate the asymptotic behaviour of the imaginary part $\mathrm{Im}\{\alpha(\omega)\}$ by combination of (30), (33) and (35) ($\omega \to \infty$):

$$\mathrm{Im}\{\alpha(\omega)\} = \frac{\eta}{\omega\rho_\mathrm{f}}\frac{\alpha_\infty}{\delta}\frac{(1/V)\int |\boldsymbol{u}_\mathrm{pw}|^2 \,\mathrm{d}S}{\langle |\boldsymbol{u}_\mathrm{p}|^2 \rangle}, \tag{38}$$

where the integration is over the pore wall surface S, and V is the pore volume. Furthermore, $\boldsymbol{u}_\mathrm{pw}$ denotes the potential flow velocity at the wall. Interpreting the averaging operation in the denominator of (38) we may write ($\omega \to \infty$)

$$\mathrm{Im}\{\alpha(\omega)\} = \alpha_\infty \tfrac{1}{2}\delta\, 2/\Lambda_2, \tag{39}$$

where the parameter Λ_2 has the dimension of length and is given by

$$\frac{2}{\Lambda_2} = \frac{\int |\boldsymbol{u}_\mathrm{pw}|^2 \,\mathrm{d}S}{\int |\boldsymbol{u}_\mathrm{p}|^2 \,\mathrm{d}V}. \tag{40}$$

Expression (40) was derived earlier by Johnson *et al.* (1987), on the basis of energy flux and energy dissipation considerations. The integration in the numerator of (40) is over the pore wall surface S; that of the denominator is over the pore volume. Thus, $2/\Lambda_2$ is essentially the surface-to-pore-volume ratio, in which each surface or volume element is weighted according to the local value of the field $\boldsymbol{u}_\mathrm{p}$. The motivation for defining Λ_2 in this way becomes apparent considering a straightforward potential flow through a cylindrical duct with radius R. As $\boldsymbol{u}_\mathrm{p}$ is the same everywhere in the duct, we easily find $\Lambda_2 = R$. The error in (39) is of $O(\delta^2)$ and thus (39) is satisfactorily accurate. Combination of (36) and (39) yields an expression for $\alpha(\omega)$ for higher frequencies with an error of $O(\delta^2)$ ($\omega \to \infty$):

$$\alpha(\omega) = \alpha_\infty\left[1 + \frac{\delta(\omega)}{\Lambda_1} + \mathrm{i}\frac{\delta(\omega)}{\Lambda_2}\right]. \tag{41}$$

The parameters Λ_1 and Λ_2, however, are not independent. Following the same reasoning as Johnson *et al.* (1987), we have the further requirement that $\alpha(\omega)$ should satisfy a symmetry relation:

$$\alpha(-\omega) = \alpha^*(\omega). \tag{42}$$

As we have $\delta(-\omega) = \mp\mathrm{i}\delta(\omega)$ we readily find from (41):

$$\Lambda_1 = \Lambda_2 = \Lambda. \tag{43}$$

This modifies (41) to ($\omega \to \infty$):

$$\alpha(\omega) = \alpha_\infty[1 + (1+\mathrm{i})\,\delta(\omega)/\Lambda]. \tag{44}$$

From (44) it becomes clear that the dynamic tortuosity $\alpha(\omega)/\alpha_\infty$ in the high-frequency regime can be characterized by the parameter δ/Λ, or, alternatively, $\nu/\omega\Lambda^2$, where ν denotes the kinematic viscosity. Consequently, we may write that the dynamic permeability, or the corresponding dynamic tortuosity, is a function of two parameters:

$$\frac{k(\omega)}{k_0} = f\left(\frac{\omega}{\omega_c}, \frac{\nu}{\omega_c \Lambda^2}\right). \tag{45}$$

This confirms the assumption by Johnson *et al.* (1987) that the dynamic permeability is a function of ω/ω_c and M. Furthermore, we have shown that the present results for α_∞, Λ_1 and Λ_2 only contain real-valued quantities that can be evaluated on the basis of steady potential flow theory. As the steady-state permeability k_0 may be computed from the Stokes flow problem, we are now able to investigate the parameter M. This has been done numerically for axisymmetrical model pores of different geometries.

4. Numerical computations

Numerical computations were performed on two different types of rotation-symmetrical pore geometries with length L, drawn in figure 1. Pore type 1 has a width W and a rotational axis P_1P_5. The surface of revolution, bounding its pore volume, is described by the generator curve $P_2P_3P_4$. It consists of line element P_3P_4 and $\frac{1}{4}$-circle segment P_2P_3, with radius R and centre C. The geometry of pore type 1 was varied in two different ways: altering R while maintaining $W = L$; altering W while maintaining $R = 0.5L$.

Using the SEPRAN finite-element package (Cuvelier, Steenhoven & Segal 1986), we computed α_∞, Λ_2 and k_0/ϕ. Results are presented in figure 2. We used relations (35) and (40), respectively, to compute α_∞ and Λ_2. In this way, we solved the potential problem $\boldsymbol{u}_0 = -\boldsymbol{\nabla}_y\psi$, where $\psi = 0$ at $z = 0$ and $\psi = 1$ at $z = -L$. Also, introducing the vector $\boldsymbol{n}$ normal to the pore walls, a Neumann-type boundary condition was prescribed at the pore walls: $\boldsymbol{n}\cdot\boldsymbol{\nabla}_y\psi = 0$. Furthermore, we computed k_0/ϕ by solving the Stokes problem $\eta\nabla_y^2\boldsymbol{u}_0 = -\boldsymbol{\nabla}p$, where $p = 0$ at $z = 0$ and $p = 1$ at $z = -L$. A Dirichlet-type boundary condition was prescribed at the pore walls: $\boldsymbol{u}_0 = \boldsymbol{0}$. For all computations, the accuracy was checked by refining the numerical grid several times.

Pore type 2 is described by generator curve $P_2P_3P_4P_5$. It consists of line-element P_4P_5 and $\frac{1}{4}$-circle segment P_2P_3, with radius R_1 and centre C_1, and $\frac{1}{4}$-circle segment P_3P_4, with radius R_2 and centre C_2. Both centres define the straight line C_1C_2 at a distance $0.5L$ from the rotational axis P_1P_6. The distance between C_1 and C_2, $d(C_1, C_2)$, is defined by the relation $d(C_1, C_2) = R_1 + R_2 = 0.75L$. The geometry of pore type 2 was varied by changing both R_1 and R_2 according to this relation. Again, we computed α_∞, Λ_2 and k_0/ϕ. Again, the accuracy was checked by grid refinement. The results of these computations are presented in figure 3. Varying this pore geometry, we achieved a perpendicular pore wall shift which enabled us to compute Λ_1, using (37). The results of this additional computation are included in figure 3(*b*). We find to a good approximation that $\Lambda_1 = \Lambda_2$, as was also theoretically expected, thus showing the reliability of our numerical methods. The results of all computations were then used to obtain the values for M, using (6). These M-values are listed in table

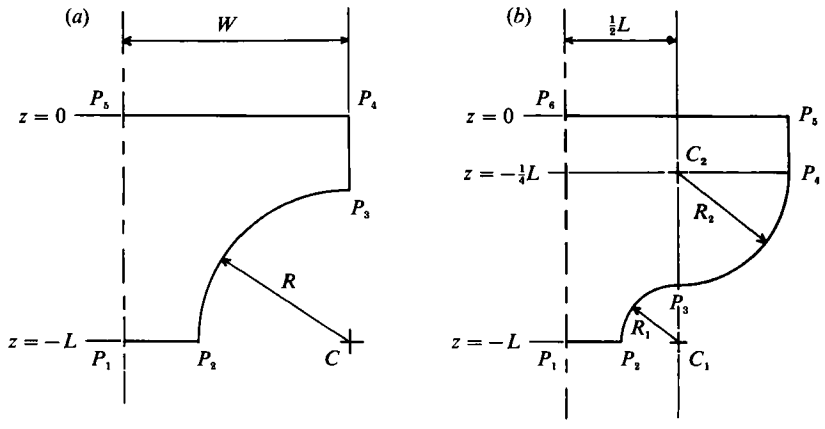

FIGURE 1. (a) Pore type 1; (b) pore type 2.

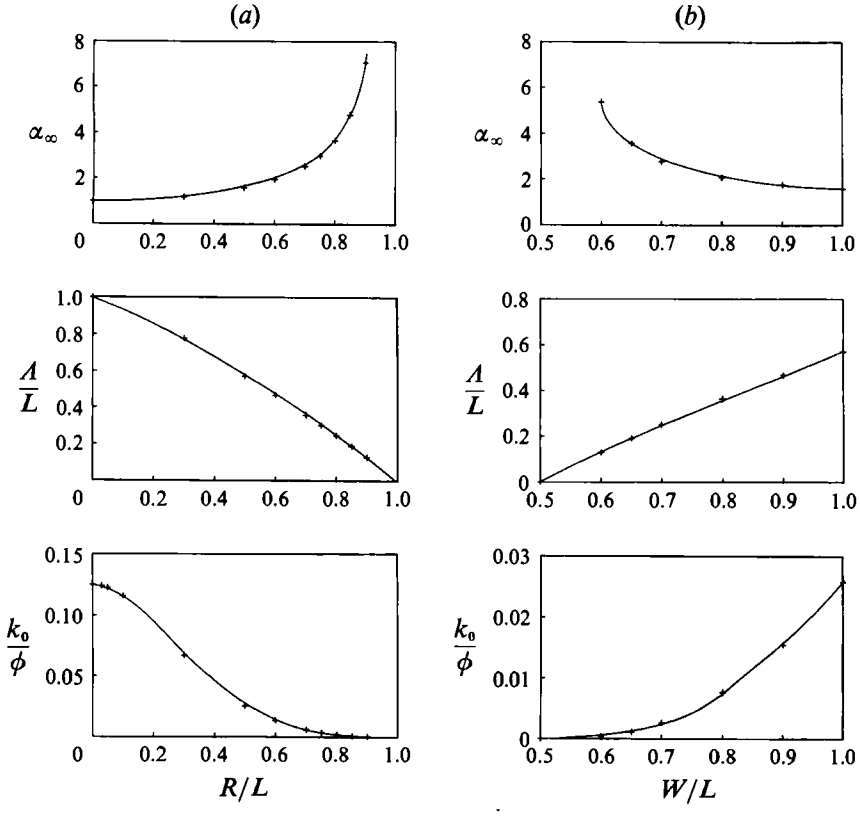

FIGURE 2. Numerical calculations of characteristic pore type 1 parameters: (a) $W/L = 1.0$, (b) $R/L = 0.5$. Λ has been calculated using the Λ_2-approach.

1. It appears that M is weakly dependent on pore geometry. The parameters R/L, W/L and R_1/L can be varied over a wide range of magnitudes without affecting M by more than about 20%. Maximum deviation from $M = 1$ is found for strongly curved pore geometries. Thus we find that many porous media satisfy the simple approximate scaling law that $k(\omega)/k_0$ is a function of only one independent parameter, ω/ω_c.

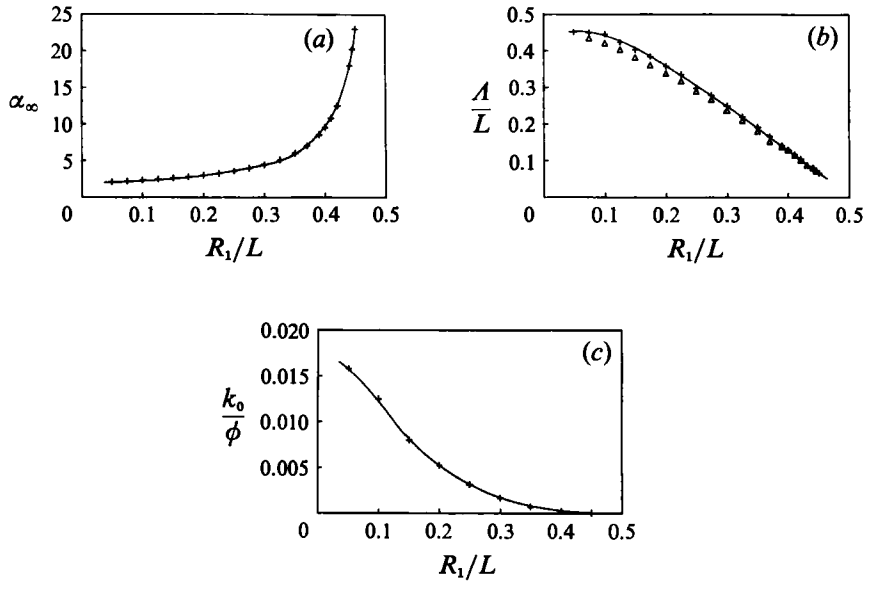

FIGURE 3. Numerical calculations of characteristic pore type 2 parameters. Λ has been calculated using both the Λ_1 ($\triangle$) and Λ_2 (+) approach.

R/L	M	W/L	M	R_1/L	M
0.3	1.04 ± 0.02	1.0	1.00 ± 0.02	0.05	1.25 ± 0.07
0.5	1.00 ± 0.02	0.9	0.99 ± 0.02	0.10	1.08 ± 0.07
0.6	0.98 ± 0.02	0.8	0.96 ± 0.02	0.15	1.03 ± 0.07
0.7	0.98 ± 0.02	0.7	0.95 ± 0.02	0.20	0.98 ± 0.05
0.75	0.97 ± 0.02	0.65	0.94 ± 0.02	0.25	0.96 ± 0.05
0.8	0.95 ± 0.02	0.6	0.93 ± 0.02	0.30	0.94 ± 0.05
0.85	0.95 ± 0.02	—	—	0.35	0.92 ± 0.05
0.9	0.93 ± 0.02	—	—	0.40	0.92 ± 0.02
—	—	—	—	0.45	0.90 ± 0.02

TABLE 1. Calculation of M-values for different pore types

5. Measurements of dynamic permeability

Auriault *et al.* (1985) were the first to report experimental data showing the transition from the viscosity-dominated low-frequency regime to the inertia-dominated high-frequency regime. We must notice that in their paper the dynamic permeability is written in the form $\eta/k(\omega) = H_1 + iH_2$. Measured data are presented for $\phi a^2 H_1/2\eta$ and $\phi H_2/\rho_f \omega$, where a is a length parameter of the porous medium. For an oscillating flow within a cylindrical duct of radius R, we find

$$a \equiv R,\ \phi a^2 H_1/2\eta \equiv 4\mathrm{Re}\{k_0/k(\omega)\}$$

and $\phi H_2/\rho_f \omega \equiv \mathrm{Re}\{\alpha(\omega)\}$. They paid particular attention to the high-frequency range. Measurements were performed on one slit-like pore geometry. In 1988, Charlaix *et al.* presented experimental data over a wide range of reduced frequencies. An oscillating flow was induced by an audio speaker, driving a latex membrane. They used small porous cylinders with lengths of 50–70 mm and diameters of 4.3 mm, consisting of sintered glass beads and sintered, crushed, glass.

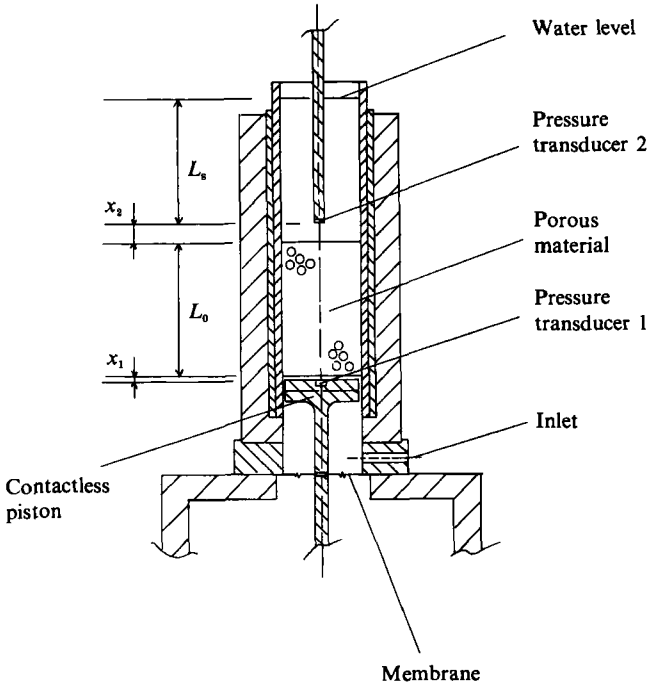

FIGURE 4. Dynamic permeability experimental set-up.

	Sample constituent	ϕ	k_0 (10^{-10} m^2)	α_∞
(i)	glass beads 0.40–0.52 mm	0.31±0.01	1.40±0.05	2.8±0.1
(ii)	glass beads 1.16–1.40 mm	0.31±0.01	9.00±0.05	2.7±0.1
(iii)	glass beads 2.50–3.50 mm	0.32±0.01	42.0±0.5	2.5±0.1
(iv)	sand grains 0.3–0.6 mm	0.29±0.01	1.00±0.05	3.1±0.1
(v)	sand grains 2.0–4.0 mm	0.31±0.03	26±1	2.8±0.3

TABLE 2. Relevant sample properties

We report here experimental data on dynamic permeability for five model porous media. We used the set-up drawn in figure 4, which had been schematically proposed by Biot (1961). The porous samples we study here are of five different particle types: (i) glass beads, size range 0.40–0.52 mm; (ii) glass beads, size range 1.16–1.40 mm; (iii) glass beads, size range 2.50–3.50 mm; (iv) sand grains, size range 0.3–0.6 mm; (v) sand grains, size range 2.0–4.0 mm. Each porous sample contains only one particle type. These particles are glued together and to the walls of a vertical brass cylinder by means of an epoxy resin, thus avoiding any free motion of the porous material. The brass cylinder has a length of 250 mm and an internal diameter of 60 mm. Each porous sample has a length L_0 of 100 mm. Porosities are measured by using the standard two-weight (dry and buoyant) method and presented in table 2. As described previously, each porous sample may be characterized by a rollover frequency ω_c, which can only be calculated after determination of the stationary permeability k_0 and the tortuosity α_∞ as described in Appendix B. Results are presented in table 2.

The sample is now carefully evacuated and the pores are filled with carbon dioxide. Then the sample is filled with degassed water until the water surface is about 20 mm

below the open upper cylinder end. Carbon dioxide is far more soluble in water than air, thus causing quick dissolution of any gas remnants. An oscillatory flow is induced by means of an MB Electronics EA 1500 permanent magnetic exciter, driving a contactless piston. The void space below the piston is bounded by a brass membrane, impermeably connected to both the cylinder wall and the piston rod. The frequency range is from 12 to 300 Hz, and so $\frac{1}{4}\lambda \gg L_0$, where we have introduced the wavelength λ. Therefore, on this scale, fluid may be regarded incompressible. The experiment is run for displacement amplitudes corresponding to Reynolds numbers usually less than 1, where Reynolds numbers are taken with respect to the mean particle diameter. Therefore, the response of the fluid to the applied pressure gradient can still be considered linear. The pressure drop across the porous sample is measured using PCB116A piezo-electric pressure transducers PT1 and PT2. PT1 is installed in the piston, whereas PT2 is mounted on the lower end of a cylindrical Perspex shaft. Signals are modified by means of Kistler 5001 amplifiers. Defining $\hat{p}_2$ as the pressure amplitude recorded by PT2, and $\hat{v}_2$ as the undisturbed fluid velocity at some distance above PT2, flow rates are deduced from the upper pressure transducer measurements:

$$-\rho_f \mathrm{i}\omega\hat{v}_2 = \hat{p}_2/L_{\mathrm{eff}}, \tag{46}$$

where we have introduced the effective fluid height L_{eff} above PT2. We computed the local flow pattern and pressure distribution in the vicinity of PT2 as a solution of the steady potential problem, using the SEPRAN finite-element package. We found $L_{\mathrm{eff}} = L_s + \Delta L$, where L_s is the length of the shaft below the fluid surface, and $\Delta L = 3.9$ mm. Introducing the macroscopic fluid velocity $\hat{v}_0$ within the porous sample, we may write a dynamic equivalent of Darcy's law:

$$\phi\hat{v}_0 = \frac{k(\omega)}{\eta}\frac{\hat{p}_h - \hat{p}_\ell}{L_0}, \tag{47}$$

where $\hat{p}_h$ and $\hat{p}_\ell$ are the fluid pressure amplitudes just below and above the porous sample, respectively. Pressures $\hat{p}_1$ and $\hat{p}_2$ though, are recorded at some distances x_1 and x_2 below and above the porous sample (see figure 4). By means of local application of continuity and momentum equations, the pressures $\hat{p}_h$ and $\hat{p}_\ell$ can be expressed in terms of the recorded pressures $\hat{p}_1$ and $\hat{p}_2$:

$$\hat{p}_h = \hat{p}_1 - \hat{p}_2(1-\beta)\,x_1/L_{\mathrm{eff}} \tag{48}$$

$$\hat{p}_\ell = \hat{p}_2[1 + (1-\beta)\,(x_2 - \Delta L)/L_{\mathrm{eff}}], \tag{49}$$

where β is the shaft-to-cylinder area ratio. Results of dynamic permeability measurements are presented in figures 5(*a*) and 5(*b*). For each porous sample, dynamic permeability and frequency are scaled by corresponding k_0 and ω_c values from table 2. In figure 5(*a*), one clearly observes the rollover of the modulus of $k(\omega)/k_0$ from the value 1 at low frequencies to a $(\omega/\omega_c)^{-1}$ dependence at high frequencies. This rollover behaviour is also clearly visible on considering the argument of $k(\omega)/k_0$ in figure 5(*b*). Errors are indicated by the size of the symbols representing the measured data. The curves in figure 5 correspond to a scaling function proposed by Johnson *et al.* (1987):

$$\frac{k(\omega)}{k_0} = \frac{1}{[1 - \frac{1}{2}\mathrm{i}M\omega/\omega_c]^{\frac{1}{2}} - \mathrm{i}\omega/\omega_c}, \tag{50}$$

where for definiteness we have chosen $M = 1$. We notice that there is good overall agreement between experiment and theory for both absolute and phase values. At

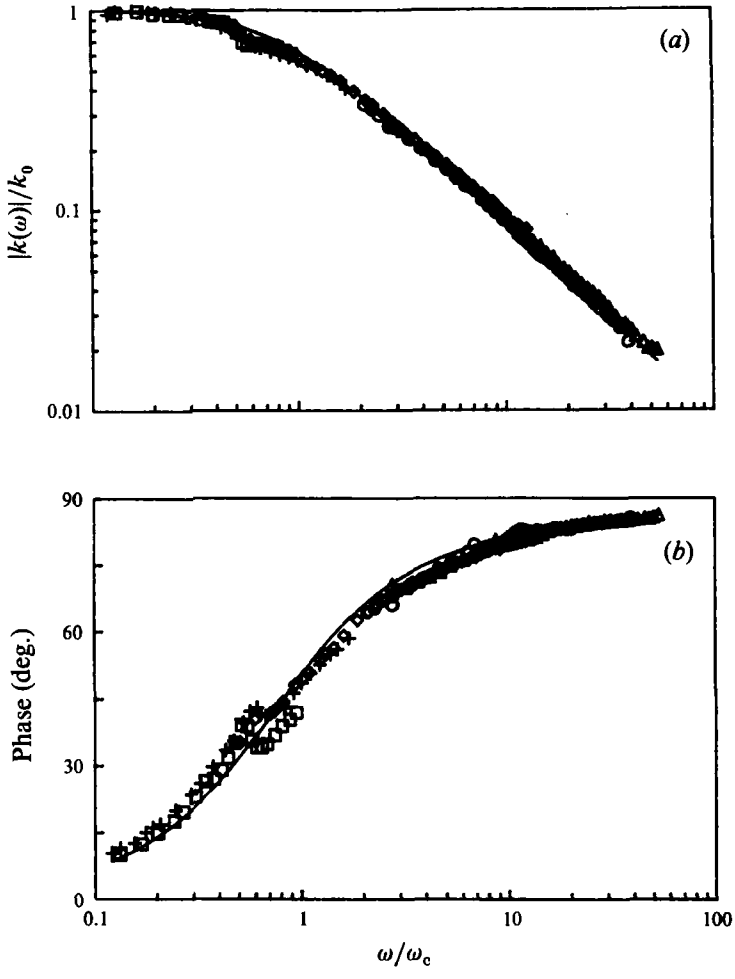

FIGURE 5. (a) Absolute values and (b) phase values of dynamic permeability measurements performed on porous samples: □, sand grains 0.3–0.6 mm; +, glass beads 0.40–0.52 mm; ◇, glass beads 1.16–1.40 mm; △, glass beads 2.50–3.50 mm; ○, sand grains 2.0–4.0 mm. The curve represents the theoretical scaling function. Errors are indicated by the size of the data symbols.

ω/ω_c-values of about 0.5, the experimentally determined absolute values of $k(\omega)/k_0$ are somewhat lower than predicted. This is caused by a persistent set-up resonance observed in the case of small particles. At the same ω/ω_c-values, this set-up resonance is also visible in the phase plot. Summarizing, we find that the present experimental results support the experiment-based conclusions of Charlaix *et al.* (1988) and the computational results of Sheng & Zhou (1988).

6. Conclusions

Our theoretical and experimental study allows the following conclusions to be drawn.

(i) We have shown that the theoretical results presented previously by Johnson *et al.* (1987) can be derived in a rigorous manner using the homogenization technique proposed by Lévy (1979), Auriault (1980) and Burridge & Keller (1981). Doing so, we derived new expressions for the real and imaginary part of the dynamic tortuosity

parameter. These are exact results, applicable over the entire frequency range. It is shown that in the high-frequency limit the macroscopic measurable dynamic permeability is described by two parameters α_∞ and Λ, characterizing the microscopic pore geometry properties. We find that it is possible to calculate Λ in two different ways, yielding the same result within limits of accuracy.

(ii) Our numerical computations support the similarity assumption of Johnson *et al.* (1987), i.e. $M \approx 1$ for several pore types, although we have observed deviations up to 20%, when calculating strongly curved pore geometries.

(iii) Experimental data are obtained by application of a new frictionless piston-induced oscillation technique. These data are all on the same curve after performing a scaling operation and are in agreement with measured data by Charlaix *et al.* (1988). This measured curve is described, within limits of accuracy, by a scaling function defined by (50), where we have chosen $M = 1$. We find that, at low ω/ω_c-values, the experimentally determined $k(\omega)/k_0$ values are slightly disturbed by a persistent set-up resonance.

This work was supported by Grant No. ETN 37.1274 of the Netherlands Foundation for Fundamental Research on Matter. We are grateful to A. A. M. Wasser for his unremitting effort in constructing and improving the experimental set-up.

Appendix A. Computation of Λ_1

In order to calculate the real part of the frequency-dependent tortuosity $\alpha(\omega)$, we have assumed the potential flow solution to be bounded by the actual pore walls, thus neglecting viscosity effects and therefore introducing an error of $O(\delta)$. We shall now present a more detailed analysis to calculate the error under consideration, by linking the actual pore velocity $\boldsymbol{u}_0$ to a potential flow solution $\boldsymbol{u}_p = -\boldsymbol{\nabla}_y \psi$. We shall choose ψ in such a way that the flow rate Q_0 corresponding to the velocity distribution $\boldsymbol{u}_0$, equals the flow rate Q, corresponding to the potential flow velocity distribution $\boldsymbol{u}_p$. We shall introduce the pore wall shift as a potential flow modifying factor.

A velocity $\boldsymbol{u}_0'$ is defined in such a way that $\boldsymbol{u}_0'$ equals $\boldsymbol{u}_0$ everywhere except in the viscous boundary layer where $\boldsymbol{u}_0'$ has a fixed value $\boldsymbol{u}_{0\delta}'$:

$$\int |\boldsymbol{u}_0|^2 \, \mathrm{d}V = \int |\boldsymbol{u}_0'|^2 \, \mathrm{d}V + \int (|\boldsymbol{u}_0|^2 - |\boldsymbol{u}_0'|^2) \, \mathrm{d}V. \tag{A 1}$$

The second term of the right-hand side of the above equation is zero, except in the boundary layer. Substituting the boundary-layer velocity distribution:

$$\boldsymbol{u}_0 = \boldsymbol{u}_{0\delta}'[1 - \mathrm{e}^{\mathrm{i}k\beta}] \tag{A 2}$$

and performing the integration in the second part of the right-hand side of (A 1) we arrive at

$$\int |\boldsymbol{u}_0|^2 \, \mathrm{d}V = \int |\boldsymbol{u}_0'|^2 \, \mathrm{d}V - \frac{\delta}{2} \int |\boldsymbol{u}_{0\delta}'|^2 \, \mathrm{d}S, \tag{A 3}$$

where S denotes the pore–grain interface surface.

Next, aiming to link $\boldsymbol{u}_0'$ to the previously defined potential flow solution $\boldsymbol{u}_p$, we note that, at constant flow rate, the presence of a viscous boundary layer of thickness δ will cause the non-viscous velocity modulus $|\boldsymbol{u}_p|$ in the whole of the pore to be lower

than $|\boldsymbol{u}_0'|$. Taking this into consideration, we write the squared velocity modulus $|\boldsymbol{u}_0'|^2$ as a Taylor series:

$$|\boldsymbol{u}_0'|^2 = |\boldsymbol{u}_\mathrm{p}|^2 + \Delta r\left[\frac{\partial}{\partial r}|\boldsymbol{u}_\mathrm{p}|^2\right]_Q + \ldots, \tag{A 4}$$

where Δr is some virtual outward displacement of the pore walls at constant flow rate and $(\partial/\partial r)\,G$ denotes the derivative of some quantity G with respect to this virtual displacement. To emphasize that the derivative is at constant flow rate, the subscript Q is added.

In order to estimate the value of Δr, we will compare the velocity distribution $\boldsymbol{u}_0'$ to the actual velocity distribution $\boldsymbol{u}_0$. We notice that the presence of the viscous boundary layer will introduce a small complex-valued flow rate difference $Q_\delta = Q_0' - Q_0$, where Q_0' is the flow rate corresponding to the velocity distribution $\boldsymbol{u}_0'$. As $|Q_\delta| \ll |Q_0'|$, we may write a first-order approximation for $|Q_0|$:

$$|Q_0| \approx |Q_0'| - \mathrm{Re}\int (\boldsymbol{u}_0' - \boldsymbol{u}_0)\cdot\boldsymbol{n}\,\mathrm{d}\beta\,\mathrm{d}l, \tag{A 5}$$

where l is a circumferential coordinate perpendicular both to the pore wall surface and the boundary-layer velocity. Furthermore, $\boldsymbol{n}$ is the normal vector defining the surface element $\mathrm{d}\beta\,\mathrm{d}l$. Substitution of (A 2) into (A 5) yields

$$|Q_0| \approx |Q_0'| - \frac{\delta}{2}\oint \boldsymbol{u}_{0\delta}'\cdot\boldsymbol{n}\,\mathrm{d}l. \tag{A 6}$$

The second term of the right-hand side of (A 6) can be interpreted as a virtual shifting of the pore walls over a distance $-\frac{1}{2}\delta$. By definition we may write $Q = Q_0$ and we may therefore conclude that $\Delta r = -\frac{1}{2}\delta$.

Now integrating (A 4) over the pore volume we arrive at

$$\int |\boldsymbol{u}_0'|^2\,\mathrm{d}V = \int |\boldsymbol{u}_\mathrm{p}|^2\,\mathrm{d}V - \frac{\delta}{2}\left[\frac{\partial}{\partial r}\int |\boldsymbol{u}_\mathrm{p}|^2\,\mathrm{d}V\right]_Q + \frac{\delta}{2}\int |\boldsymbol{u}_\mathrm{pw}|^2\,\mathrm{d}S. \tag{A 7}$$

In (A 3) we may replace $\boldsymbol{u}_{0\delta}'$ by the potential flow velocity at the wall $\boldsymbol{u}_\mathrm{pw}$ without loss of accuracy, i.e. accepting an error of $O(\delta^2)$. This is easily seen by writing $|\boldsymbol{u}_{0\delta}'|^2$ as a Taylor series also. Subsequent substitution of (A 7) into (A 3) yields a relation between the actual pore velocity distribution $\boldsymbol{u}_0$ and the potential flow velocity distribution $\boldsymbol{u}_\mathrm{p}$:

$$\int |\boldsymbol{u}_0'|^2\,\mathrm{d}V = \int |\boldsymbol{u}_\mathrm{p}|^2\,\mathrm{d}V - \frac{\delta}{2}\left[\frac{\partial}{\partial r}\int |\boldsymbol{u}_\mathrm{p}|^2\,\mathrm{d}V\right]_Q. \tag{A 8}$$

Dividing the entire equation (A 8) by the pore volume V and by the squared macroscopic velocity modulus $|\boldsymbol{v}_0|^2$, we find that the left-hand side is the real part of the dynamic tortuosity $\mathrm{Re}\,(\alpha)$, and that the first term of the right-hand side is the extreme high-frequency limit of the dynamic tortuosity α_∞. From (A 8) we write

$$\mathrm{Re}\,(\alpha) = \alpha_\infty[1 + \tfrac{1}{2}\delta\,2/\Lambda_1], \tag{A 9}$$

where the parameter Λ_1 has the dimension of length and is given by

$$\frac{2}{\Lambda_1} = \frac{-\left[(\partial/\partial r)\int |\boldsymbol{u}_\mathrm{p}|^2\,\mathrm{d}V\right]_Q}{\int |\boldsymbol{u}_\mathrm{p}|^2\,\mathrm{d}V}. \tag{A 10}$$

Equation (A 10) offers the opportunity for numerical computation of the value of A_1 by shifting the pore walls while maintaining constant flow rate by adapting the flow potential difference $\Delta\psi$ between two equipotential surfaces. This rather laborious procedure may be simplified considerably by writing

$$-\left[\frac{\partial}{\partial r}\int|\boldsymbol{u}_\mathrm{p}|^2\,\mathrm{d}V\right]_Q=\left[\frac{\partial}{\partial r}\int|\boldsymbol{u}_\mathrm{p}|^2\,\mathrm{d}V\right]_{\Delta\psi}. \tag{A 11}$$

The differentiation at constant flow rate has now been replaced by a more convenient differentiation at constant flow potential difference. We shall prove (A 11) by considering an incompressible flow at microscale

$$\nabla_y\cdot(\psi\nabla_y\psi)=|\boldsymbol{u}_\mathrm{p}|^2. \tag{A 12}$$

Integration over the pore volume and application of Gauss' theorem yields

$$\oint\psi(\boldsymbol{u}_\mathrm{p}\cdot\boldsymbol{n})\,\mathrm{d}A=\int|\boldsymbol{u}_\mathrm{p}|^2\,\mathrm{d}V, \tag{A 13}$$

where A is the integrating surface consisting of pore wall surfaces and two arbitrary bounding equipotential surfaces. Furthermore, $\boldsymbol{n}$ is the normal vector defining a surface element $\mathrm{d}A$. As $\boldsymbol{u}_\mathrm{p}\cdot\boldsymbol{n}=0$ at the pore wall surfaces, we arrive at

$$\int|\boldsymbol{u}_\mathrm{p}|^2\,\mathrm{d}V=Q\,\Delta\psi. \tag{A 14}$$

We now take the derivative with respect to r of (A 14) at constant flow rate:

$$\left[\frac{\partial}{\partial r}\int|\boldsymbol{u}_\mathrm{p}|^2\,\mathrm{d}V\right]_Q=Q\left[\frac{\partial\Delta\psi}{\partial r}\right]_Q=-Q\frac{[\partial Q/\partial r]_{\Delta\psi}}{[\partial Q/\partial\Delta\psi]_r}. \tag{A 15}$$

At constant r, i.e. not changing the pore geometry, we may write

$$[\partial Q/\partial\Delta\psi]_r=Q/\Delta\psi. \tag{A 16}$$

By substitution of (A 16) into (A 15), we finally arrive at (A 11).

Appendix B

B.1. *Determination of* k_0

Stationary permeability properties of the porous samples within their containing brass cylinders are measured in a gas flow set-up, drawn in figure 6. It consists of two pressure chambers connected via the porous sample. Flow rates are varied by modifying the upstream pressure, and measured by means of a gasmeter. (Meterfabriek Dordrecht, Natte precisie gasmeter, Type 1). The pressure drop across the sample is measured, using a highly sensitive water manometer (v. Essen, Betz micromanometer, 500 mm). As pressure drops appear to be very small, compressibility effects are ignored throughout. For low velocities the Darcy law holds:

$$\partial p/\partial x=-(\eta/k_0)\,(Q/A), \tag{B 1}$$

where A is the total cross-sectional area of the porous sample and Q is the flow rate. For higher velocities, the Darcy law has to be extended by an extra term proportional to the flow rate squared:

$$\partial p/\partial x=-(\eta/k_0A)\,Q+bQ^2, \tag{B 2}$$

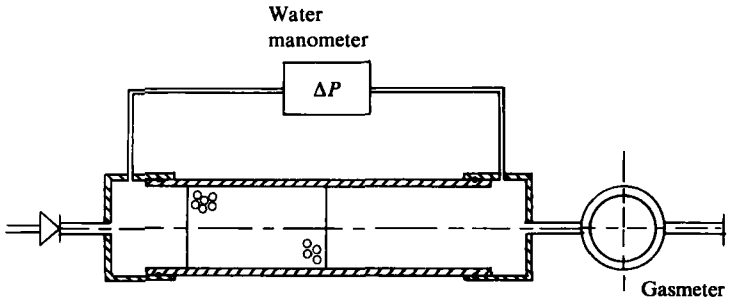

FIGURE 6. Experimental set-up for stationary permeability measurements by means of air flow.

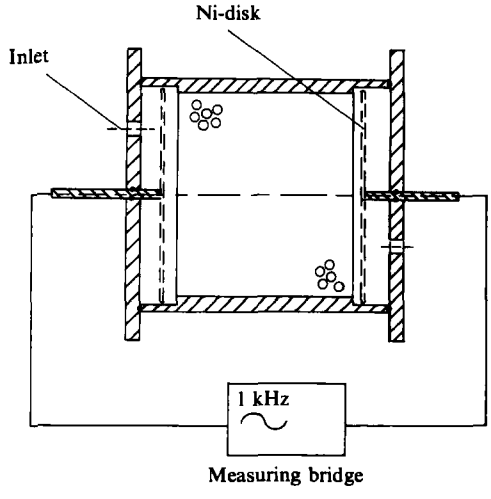

FIGURE 7. Experimental set-up for measuring the electrical conductivity of a porous electrolyte-saturated insulator.

where b is an arbitrary phenomenological constant. This relation is often referred to as Forchheimer's law. Measurements are performed for all pore types, and best-fit Forchheimer curves are subsequently calculated.

B.2. *Determination of* α_∞

The tortuosity is determined in an electrical conductivity experiment. The analogy between the acceleration of an inviscid incompressible fluid within a rigid porous medium, and the electrical current density within an electrolyte-filled porous insulator, was first demonstrated by Brown (1980). Later this analogy was also discussed by Johnson & Sen (1981), and experimentally verified by Johnson *et al.* (1982). We may write:

$$\alpha_\infty = \phi \sigma_f / \sigma, \tag{B 3}$$

where σ is the conductivity of the fluid-filled porous insulator, and σ_f is the intrinsic fluid conductivity.

The experimental set-up is drawn in figure 7. For obvious conductivity reasons, the samples within their containing brass cylinders could not be used. Five new samples were prepared in an identical way within Perspex cylinders with a length of 85 mm and an internal diameter of 70 mm. Each porous sample has a length L_1 of 60 mm. The electrodes, consisting of porous Ni-disks, are placed on both sides against

the porous sample, which has previously been saturated with a degassed 0.01 mol/l KCl saline solution. Conductivity is measured, using a resistance bridge (Marconi Universal Bridge TF2700). In order to avoid electrolysis, all conductivities are measured using a.c. with a 1000 Hz frequency.

REFERENCES

AURIAULT, J. L. 1980 Dynamic behaviour of a porous medium saturated by a Newtonian fluid. *Intl J. Engng Sci.* **18**, 775–785.

AURIAULT, J. L., BORNE, L. & CHAMBON, R. 1985 Dynamics of porous saturated media, checking of the generalized law of Darcy. *J. Acoust. Soc. Am.* **77**, 1641–1650.

BEAR, J. & BACHMAT, Y. 1990 *Introduction to Modeling of Transport Phenomena in Porous Media.* Kluwer.

BEASLEY, J. D. & TORQUATO, S. 1988 New bounds on the permeability of a random array of spheres. *Phys. Fluids* A **1**, 199–207.

BIOT, M. A. 1961 Generalized theory of acoustic propagation in porous dissipative media. *J. Acoust. Soc. Am.* **34**, 1254–1264.

BROWN, R. J. S. 1980 Connection between formation factor for electrical resistivity and fluid–solid coupling factor in Biot's equation for acoustic waves in fluid-filled porous media. *Geophys.* **45**, 1269–1275.

BURRIDGE, R. & KELLER, J. B. 1981 Poroelasticity equations derived from microstructure. *J. Acoust. Soc. Am.* **70**, 1140–1146.

CHARLAIX, E., KUSHNICK, A. P. & STOKES, J. P. 1988 Experimental study of dynamic permeability in porous media. *Phys. Rev. Lett.* **61**, 1595–1598.

CUVELIER, C., STEENHOVEN, A. A. VAN & SEGAL, G. 1986 *Finite Element Methods and Navier–Stokes Equations.* Reidel.

JOHNSON, D. L. 1989 Scaling function for dynamic permeability in porous media. *Phys. Rev. Lett.* **63**, 580.

JOHNSON, D. L., KOPLIK, J. & DASHEN, R. 1987 Theory of dynamic permeability and tortuosity in fluid-saturated porous media. *J. Fluid Mech.* **176**, 379–402.

JOHNSON, D. L., PLONA, T. J., SCALA, C., PASIERB, F. & KOJIMA, H. 1982 Tortuosity and acoustic slow waves. *Phys. Rev. Lett.* **49**, 1840–1844.

JOHNSON, D. L. & SEN, P. N. 1981 Multiple scattering of acoustic waves with application to the index of refraction of fourth sound. *Phys. Rev.* B **24**, 2486–2496.

LANDAU, L. D. & LIFSHITZ, E. M. 1959 *Fluid Mechanics.* Pergamon.

LARSON, R. E. & HIGDON, J. J. L. 1989 A periodic grain consolidation model of porous media. *Phys. Fluids* A **1**, 38–46.

LÉVY, T. 1979 Propagation of waves in a fluid-saturated porous elastic solid. *Intl J. Engng Sci.* **17**, 1005–1014.

MEI, C. C. & AURIAULT, J. L. 1991 The effect of weak inertia on flow through a porous medium. *J. Fluid Mech.* **222**, 647–663.

RUBENSTEIN, J. & TORQUATO, S. 1989 Flow in random porous media: mathematical formulation, variational principles and rigorous bounds. *J. Fluid Mech.* **206**, 25–46.

SHENG, P. & ZHOU, M.-Y. 1988 Dynamic permeability in porous media. *Phys. Rev. Lett.* **61**, 1591–1594.

SHENG, P., ZHOU, M. Y., CHARLAIX, E., KUSHNICK, A. P. & STOKES, J. P. 1989 Reply to Johnson, D. L. 1989 Scaling function for dynamic permeability in porous media. *Phys. Rev. Lett.* **63**, 581.

YAVARI, B. & BEDFORD, A. 1990 The Biot drag and virtual mass coefficient for face centered cubic granular materials. *Intl J. Multiphase Flow* **16**, 885–897.